Check for updates

Tribenzyl Organic Cations Carried Multidentate X-Type Lewis Soft Base for High-Performance Foldable Perovskite Light-Emitting Diodes

*Benzheng Lyu, Dongyu Li, Chengxuan Ke, Haoquan Liang, Jiayun Sun, Qi Xiong, John Jinwook Kim, Yanning Zhang, Guangfu Luo, and Wallace C. H. Choy**

Lead-halide perovskite nanocrystals (PNCs) exhibit significant potential for advancing foldable perovskite light-emitting diodes (*F*-PLEDs) due to their discrete crystalline morphology, bright emission across an extensive color gamut, and remarkable color purity; however, their progression remains in the early stages with the concerns of inadequate performance and mechanical instability. This study proposes a ligand strategy employing tribenzyl organic cation (tribenzylamine, TBA) carried multidentate X-type Lewis soft base (sodium acid pyrophosphate, SAPP) to address the challenges above simultaneously. Specifically, the use of multibranched aromatic ligands considerably improved the adhesion force between PNCs and adjacent layers, enhancing mechanical stability during folding, while the control sample shows deleterious cracks. Additionally, TBA-SAPP ligands effectively eliminate the defects in PNC film, yielding exceptional photoluminescence properties with a near-unity quantum yield. Consequently, the multifunctional ligands improved *F*-PLEDs to achieve a record-high external quantum efficiency (EQE) of 16.2% compared to the previously reported pure-red flexible PLEDs and display substantially improved spectral and operational stability. Equally important, these devices demonstrate robust mechanical properties, enduring a small folding radius of 1 mm for 5000 cycles. This ligand strategy is anticipated to inspire relevant research in PNCs and promote the realization of highly efficient and mechanically stable *F*-PLEDs.

1. Introduction

Lead-halide perovskite nanocrystals (PNCs) possess inherent independent nanocrystalline characteristics, coupled with bright emission, wide color gamut coverage, and high color purity, showcasing the tremendous potential for applications in the field of foldable light-emitting diodes (*F*-PLEDs) with broad utility in foldable smartphones, robotics, and next-generation wearable display devices, etc.[1–3] From a mechanical perspective, the independent nanocrystalline morphology (≈10 nm in size) effectively prevents brittle damage to the inorganic emitting layer during folding processes.[4] Nonetheless, current state-of-the-art *F*-PLEDs urgently require improvements in mechanical stability, potentially due to the insufficient interlayer and intralayer adhesion of PNCs, which is attributed to the weak van der Waals forces resulting from the alkyl chains of traditional oleic acid (OA) and oleylamine (OAm) ligands.[5–7] Given that the neighboring carrier transport layer of PNCs often

---

B. Lyu, D. Li, J. Sun, Q. Xiong, J. J. Kim, W. C. H. Choy
Department of Electrical and Electronic Engineering
the University of Hong Kong
Hong Kong, P. R. China
E-mail: chchoy@eee.hku.hk

C. Ke, G. Luo
Department of Materials Science and Engineering
Southern University of Science and Technology
Shenzhen 518055, P. R. China

C. Ke, G. Luo
Institute of Innovative Materials
Southern University of Science and Technology
Shenzhen 518055, P. R. China

C. Ke, G. Luo
Guangdong Provincial Key Laboratory of Computational Science and Material Design
Southern University of Science and Technology
Shenzhen 518055, P. R. China

C. Ke
Department of Materials Science and Engineering
City University of Hong Kong
Kowloon, Hong Kong, P. R. China

H. Liang, Y. Zhang
Institute of Fundamental and Frontier Sciences
University of Electronic Science and Technology of China
Chengdu 611731, P. R. China

The ORCID identification number(s) for the author(s) of this article can be found under https://doi.org/10.1002/adma.202415211

© 2025 The Author(s). Advanced Materials published by Wiley-VCH GmbH. This is an open access article under the terms of the Creative Commons Attribution-NonCommercial License, which permits use, distribution and reproduction in any medium, provided the original work is properly cited and is not used for commercial purposes.

DOI: 10.1002/adma.202415211

comprises organic semiconductors containing abundant aromatic groups,[8] utilizing aromatic ligands is expected to effectively enhance the adhesion force between PNCs and adjacent layers, thereby improving the mechanical robustness of *F*-PLEDs.[9,10]

On the other hand, PNCs can achieve primary colors that comply with International Telecommunication Union - Radiocommunication Sector Recommendation BT.2100 (Rec.2100) standards through mixed-halide or strong quantum confinement effects.[11–14] Although mixed-halide nanocrystals exhibit larger sizes, reducing specific surface areas and defects compared to their smaller-sized single-halide quantum dot counterparts, defect passivation remains a critical obstacle to device performance and operational lifetime. Moreover, defects can accelerate phase segregation, significantly undermining spectral stability.[15] The primary defect of PNCs is the uncoordinated Pb^{2+} species present on the surface, which is a Lewis soft acid, and X-type Lewis soft base ligands have demonstrated superior passivation effects compared to other Z- and L- type ligands or hard base ligands.[16–18] Alongside the impressive synergistic effect of multidentate ligands,[19,20] we propose multidentate X-type Lewis soft base as the most suitable ligands option. To the best of our knowledge, such ligands have not been employed in PNCs-related research thus far, possibly due to the high degree of ionization of X-type Lewis soft base and the high negative charge density of multidentate anions, significantly impeding the solubility of the ligand in the non-polar PNCs dispersion.

In this study, we demonstrate that the utilization of tribenzyl organic cation (tribenzylamine, TBA) carried multidentate X-type Lewis soft base (sodium acid pyrophosphate, SAPP) simultaneously address the challenges of mechanical instability and defect passivation in *F*-PLEDs. Multiple characterizations confirm that both TBA and SAPP can successfully interact with PNCs after the ligand exchange process. Remarkably, this approach effectively enhances the adhesion between PNCs and adjacent layers, thereby suppressing crack formation during flexible testing under a small folding radius of 1 mm. Moreover, a low-defect PNCs thin film was realized, exhibiting excellent photoluminescence (PL) properties with PLQY reaching 96.1%, low nonradiative recombination rate, and high exciton binding energy. Finally, the successfully fabricated *F*-PLEDs demonstrate an EQE of up to 16.2% and showcase good spectral stability and operational stability (T_{50}≈216 min), alongside robust mechanical properties capable of withstanding a small folding radius of 1 mm for 5000 cycles. Consequently, this work paves the way for the application of multibranched aromatic cation carriers and multidentate X-type Lewis soft base ligands in the PNCs area, thereby promoting the practical implementation of *F*-PLEDs.

2. Results and Discussion

Figure S1 (Supporting Information) illustrates the chemical structure of the TBA and SAPP, which coalesce through a high-temperature proton exchange reaction to form TBA-SAPP, hereinafter referred to as TS (left panel of **Figure** 1a). The multibranched non-polar aromatic rings of TBA enable the product TS to dissolve in toluene, and this ligand structure is also expected to facilitate the dispersion of PNCs. Control pure-red PNCs (C-PNCs) with traditional OA and OAm ligands were synthesized employing a thermal injection approach with mixed Br/I precursors.[21] By implementing the ligands exchange process, TBA-, SAPP-, and TS-PNCs were respectively obtained (details in the Methods section). The density functional theory (DFT) calculations were performed to elucidate the interaction mechanism between TBA and SAPP with the PNC surface. As depicted in the latter part of Figure 1a, SAPP participates in synergistic coordination interactions with the adjacent dangling Pb^{2+} ions of PNCs, while the ammonium ions of TBA interact with halide ions and the phenyl rings also establish coordination bonds with Pb^{2+} ions. Both SAPP and TBA demonstrate significant interactions with the PNCs, marked by high adsorption energies (E_{ads}) exceeding 3 eV, notably surpassing the E_{ads} values associated with conventional OA and OAm ligands (≈1.5 eV).[22,23]

Figure 1b delineates the chemical composition of TS-PNCs with aromatic ligands and also their neighboring layers, inclusive of electron transport layer 2,2′,2″-(1,3,5-benzinetriyl)-tris(1-phenyl-1-H-benzimidazole) (TPBi) and hole transport layer poly(4-butylphenyl-diphenyl-amine) (poly-TPD), both containing large conjugated organic units.[24,25] The multibranched aromatic ligands enhance both interlayer and intralayer adhesion through π–π interaction, which is beneficial to improving mechanical stability. Conversely, as illustrated in Figure S2 (Supporting Information), since the surface of C-PNCs is coated with OA and OAm, the van der Waals forces between the long alkyl chains and adjacent layers are considerably weak. To quantitatively ascertain the impact of different ligands on the interfacial adhesion between PNCs and adjacent layers, the adhesion force is measured with atomic force microscopy (AFM).[26] A schematic of the AFM measurement setup is depicted in the inset of Figure 1c, where the AFM tips are coated with TPBi or poly-TPD. To simulate the PNCs layers in *F*-PLEDs, a fluorinated colorless polyimide (cPI) semi-embedded Ag nanonetwork (AgNW) and layers of poly(3,4-ethylenedioxythiophene):polystyrene sulfonate (PEDOT:PSS), poly-TPD, and PNCs were sequentially prepared.[27,28] As the tips slowly approached and retracted from the PNC surface, typical force-displacement plots were obtained (Figures S3 and S4, Supporting Information), and the extracted adhesion forces were summarized in Figure 1c. The average adhesion forces of C-PNCs with TPBi and poly-TPD were 0.20 and 1.17 nN, respectively; this difference may be due to the molecular and polymeric nature of TPBi and poly-TPD. The adhesion forces of SAPP-PNCs were found to be very close to those of C-PNCs, likely due to the insolubility of SAPP in toluene. Adhesion forces of TBA-PNCs with TPBi and poly-TPD increased significantly to 0.25 and 1.73 nN, respectively. Similarly, the adhesion forces of TS-PNCs with TPBi and poly-TPD showed a notable improvement to 0.34 and 2.13 nN, respectively, surpassing those of the C-PNCs coated with long alkyl chain ligands. The lower adhesion forces of TBA-PNCs compared to TS-PNCs can be attributed to the weak binding of deprotonated TBA to the PNC surface (Figure S5, Supporting Information). Adhesion forces measured using bare silicon AFM tips further corroborated the substantial enhancement in adhesion forces with TS ligands (Figures S6 and S7, Supporting Information). The surface topographies of various PNC films were also characterized via AFM as shown in Figure S8 (Supporting Information). The slightly increased root-mean-squared roughness (RMS) can be attributed to the enhanced intralayer adhesion of PNCs.

© 2025 The Author(s). Advanced Materials published by Wiley-VCH GmbH

15214095, 2025, 25, Downloaded from https://advanced.onlinelibrary.wiley.com/doi/10.1002/adma.202415211, Wiley Online Library on [03/09/2025]. See the Terms and Conditions (https://onlinelibrary.wiley.com/terms-and-conditions) on Wiley Online Library for rules of use; OA articles are governed by the applicable Creative Commons License

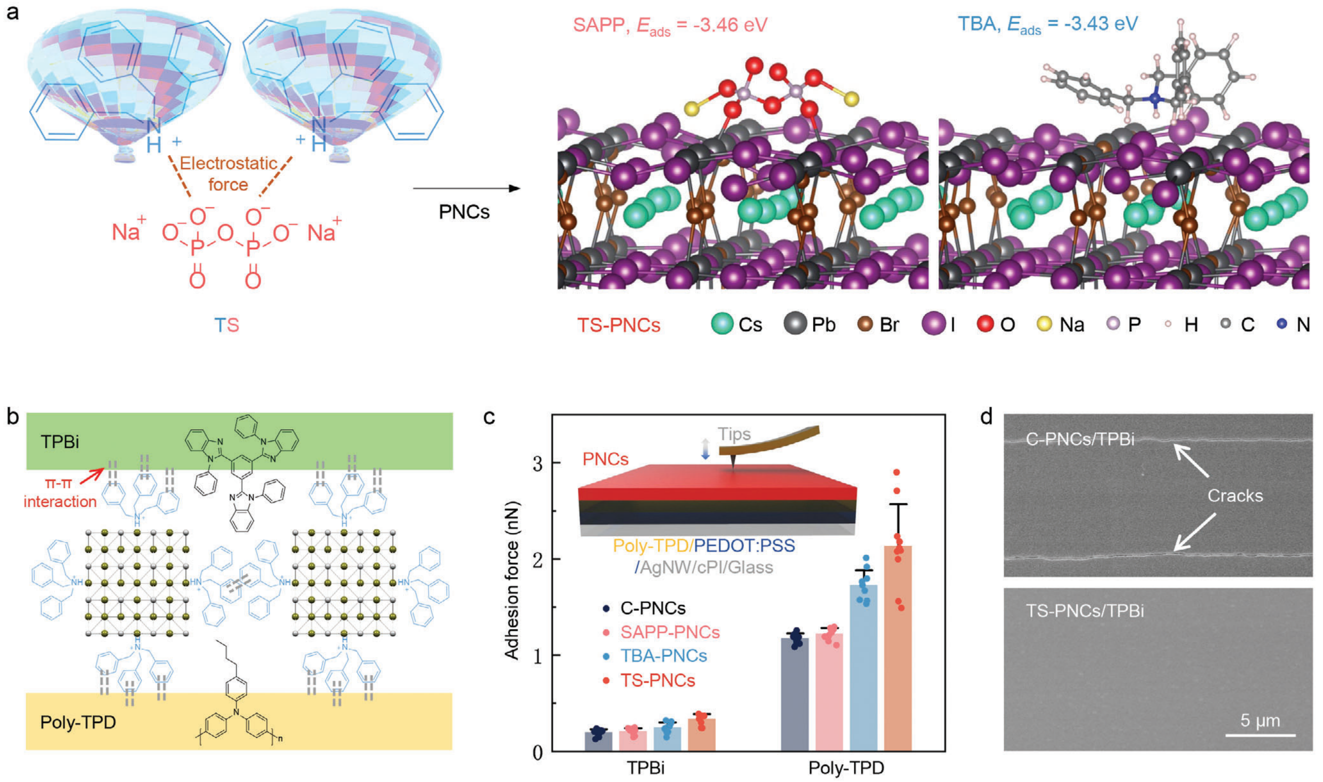

Figure 1. a) Chemical structure of TS ligands, the optimized configuration structure, and E_{ads} of the ligands interacting with PNCs based on DFT calculation. TBA with multiple aromatic branching structures acts like a hot air balloon to facilitate the dissolution of SAPP in toluene. b) Schematic diagram of TS-PNCs with aromatic ligands and neighboring layers, including electron transport layer TPBi and hole transport layer poly-TPD. c) Schematic of the AFM measurement setup (insert) and summary of extracted adhesion forces. d) SEM imaging of C- and TS-PNCs/TPBi films after mechanical folding test.

Furthermore, the AgNW/PEDOT:PSS/poly-TPD/PNCs/TPBi structure was fabricated and subjected to 5000 folding cycles at a small radius of 1 mm. Figure S9 (Supporting Information) presents the digital photographs of the mechanical folding test. Subsequently, the morphology of the films was investigated using scanning electron microscope (SEM) imaging (Figure 1d). In the composite films of C-PNCs, noticeable cracks were observed, which are highly detrimental to flexible devices. In contrast, the composite films of TS-PNCs exhibited significantly reduced cracking, attributed to the enhanced interlayer and intralayer interactions provided by the TS ligands. To further understand the underlying mechanisms behind the enhanced mechanical properties of TS ligands, two adjacent units containing PNCs and TBA were constructed and simulated to explore possible configurations during folding tests (Figure S10, Supporting Information). Additionally, PNCs with OAm ligands were utilized as reference samples (Figure S11, Supporting Information) to assess the influences of ligands on system energy with varying distances. As illustrated in Figure S12 (Supporting Information), the energy curve for the system with OAm exhibited a broader profile compared to the system with TBA, attributed to the weaker interactions between OAm. The Young's modulus of the interfacial ligands extracted from the energy curves revealed that TBA exhibited a significantly higher Young's modulus (166.6 MPa) than OAm (39.9 MPa). Furthermore, utilizing these mechanical properties along with Young's modulus of $CsPbBr_{1.2}I_{1.8}$ (16 GPa), finite element analysis was conducted to investigate the mechanical behavior of the PNC/ligands/PNC system under external forces (Figure S13, Supporting Information). The results indicate that the strain within the interfacial ligands is notably higher than in the PNC regions (white color), and OAm (orange) displayed much higher strain levels compared to TBA (yellow). The interfacial strain-relative expansion relationship was plotted in the right panel of Figure S13 (Supporting Information). Consequently, the use of TS ligands effectively improved mechanical stability in the folding tests, thereby facilitating the development of stable *F*-PLEDs.

Regarding the chemical and physical structures of as-synthesized PNCs, multiple characterization techniques were employed for investigation. **Figure 2a** illustrates scanning transmission electron microscopy (STEM) images of both C- and TS-PNCs across a broad area, revealing markedly different stacking and arrangement behaviors. C-PNCs, coated with long alkyl chain ligands, exhibit a rather dispersed and isolated arrangement, whereas TS-PNCs display a more densely packed structure, indicative of augmented adhesion due to the presence of TS ligands. The corresponding size distributions and Gaussian fits of TS-PNCs are consolidated in Figure S14 (Supporting Information), disclosing an average particle size of ≈12.0 nm. High-resolution STEM (HR-STEM, Figure S15, Supporting Information) of TS-PNCs exhibits the (110) plane with a lattice spacing of 0.608 nm. Figure 2b presents the energy dispersive X-ray

© 2025 The Author(s). Advanced Materials published by Wiley-VCH GmbH

15214095, 2025, 25, Downloaded from https://advanced.onlinelibrary.wiley.com/doi/10.1002/adma.202415211, Wiley Online Library on [03/09/2025]. See the Terms and Conditions (https://onlinelibrary.wiley.com/terms-and-conditions) on Wiley Online Library for rules of use; OA articles are governed by the applicable Creative Commons License

15214095, 2025, 25, Downloaded from https://advanced.onlinelibrary.wiley.com/doi/10.1002/adma.202415211, Wiley Online Library on [03/09/2025]. See the Terms and Conditions (https://onlinelibrary.wiley.com/terms-and-conditions) on Wiley Online Library for rules of use; OA articles are governed by the applicable Creative Commons License

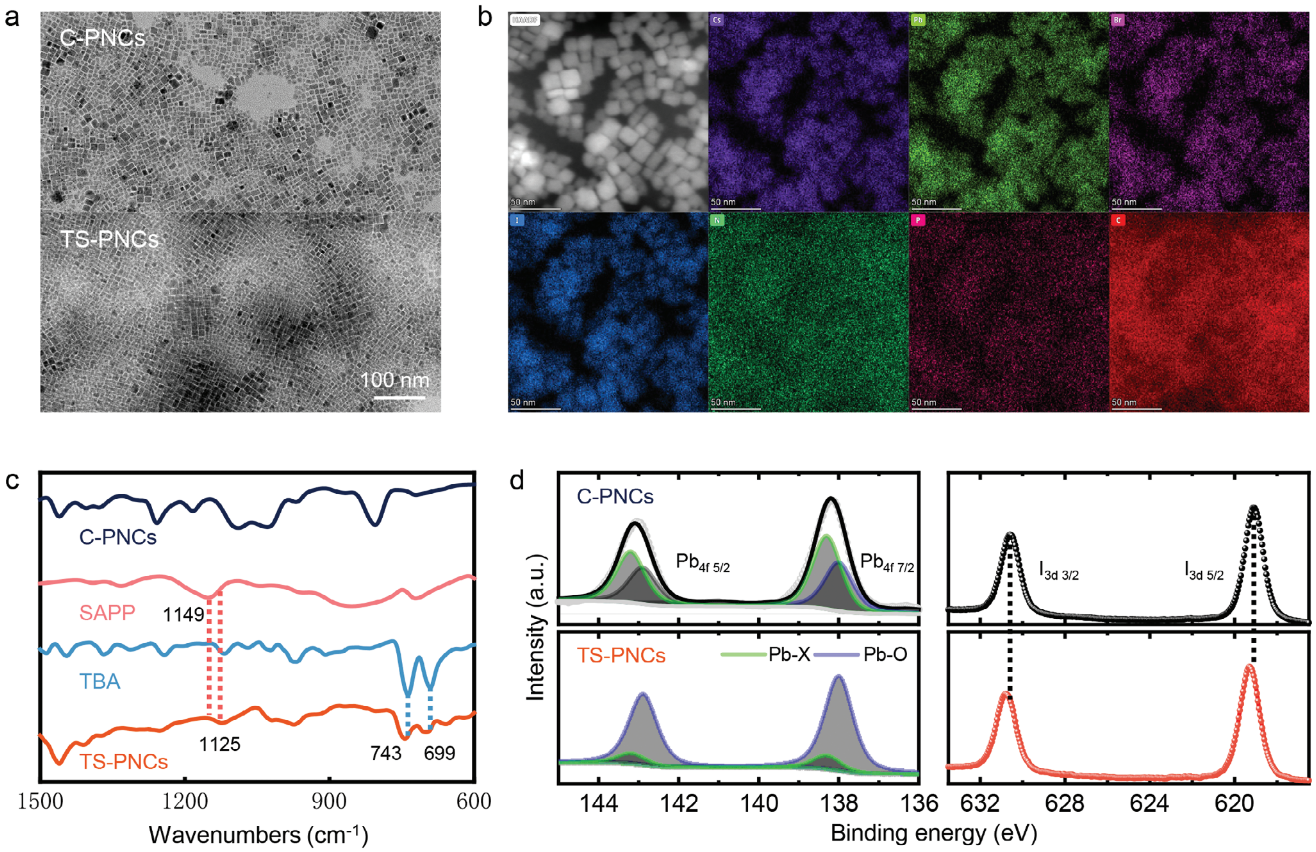

Figure 2. a) STEM images of C- and TS-PNCs. b) EDX mapping of TS-PNCs. c) ATR-FTIR spectrum of C-PNCs, SAPP, TBA, and TS-PNCs. d) Core levels of Pb 4f and I 3d in XPS.

spectroscopy (EDX) mapping of TS-PNCs, including high-angle annular dark-field imaging (HAADF), as well as the distribution of various individual elements. The mapping of Cs, Pb, Br, and I elements verifies the composition of PNCs, while the enrichment of N and P elements coinciding with the PNCs region substantiates the successful attachment of both TBA and SAPP with PNCs. Quantitively, both C- and TS-PNCs boast a near-perfect ABX_3 perovskite composition as shown in Table S1 and Figure S16 (Supporting Information), and the P/Pb ratio in TS-PNCs reaches up to 5.1%. Given the previously determined average particle size of 12.0 nm and lattice constant of 0.608 nm, the surface Pb ratio is calculated as 30.4%, and 33.6% of the surface Pb is passivated by SAPP which is a remarkably high proportion considering that some of the surface Pb interact with halogen or oleic acid. X-ray diffraction (XRD) patterns exhibit three primary peaks positioned approximately at 15.1°, 21.2°, and 29.9°, corresponding to the (110), (111), and (220) crystal planes of tetragonal phase PNCs (Figure S17, Supporting Information).[29] The significant enhancement of (111) peak and the slightly enhanced (110) and (220) peaks suggest a superior crystal arrangement for TS-PNCs,[30] in alignment with the dense arrangement observed in STEM. The interaction between TS and PNCs was further corroborated through attenuated total reflection Fourier transform infrared spectroscopy (ATR-FTIR) measurements, as depicted in Figure 2c. The typical pyrophosphate stretching vibrations at 1149 cm^{-1} were observed in sample SAPP and shifted to 1124 cm^{-1} in TS-PNCs due to the formation of P-O-Pb bonds.[31–33] In addition, the out-of-plane C-H bending characteristic peaks of TBA were located at 736 and 692 cm^{-1}, while similar feature pairs were also observed in TS-PNCs, which were red-shifted to 743 and 699 cm^{-1}, confirming the presence of TBA and its interaction with PNCs.[34] High-resolution X-ray photoelectron spectroscopy (XPS) was employed to analyze the chemical environment of individual atoms. Figure 2d and Figure S18 (Supporting Information) display the core levels of Pb 4f, I 3d, and Br 3d. The Pb 4f peaks demonstrate a clear trend toward low binding energy. By fitting the Pb 4f peaks as Pb-X and Pb-O, which represent the surface Pb binding with halides and ligands on the PNCs, respectively, the proportion of Pb-O in TS-PNCs increases significantly due to the coordination bond between SAPP and Pb.[35,36] Conversely, the halide peaks shift toward higher binding energy due to electrostatic and hydrogen bonding interactions between TBA and the halide.[37–39] The presence of SAPP was also confirmed by the P 2p peak in Figure S19 (Supporting Information), and the peak at around 530.8 eV in the O 1s spectra illustrates the formation of a stable chemical bond between the oxygen in SAPP and Pb in PNCs.[40] The relatively weak N 1s signal in Figure S20 (Supporting Information) can be attributed to the cation loss during the extended high-vacuum treatment before XPS analysis,[41] and there are no apparent changes in the peaks of Cs 3d and C 1s. Moreover, the influence of TS ligands on the energy band of PNCs is minimal, which is substantiated by ultraviolet

© 2025 The Author(s). Advanced Materials published by Wiley-VCH GmbH

15214095, 2025, 25, Downloaded from https://advanced.onlinelibrary.wiley.com/doi/10.1002/adma.202415211, Wiley Online Library on [03/09/2025]. See the Terms and Conditions (https://onlinelibrary.wiley.com/terms-and-conditions) on Wiley Online Library for rules of use; OA articles are governed by the applicable Creative Commons License

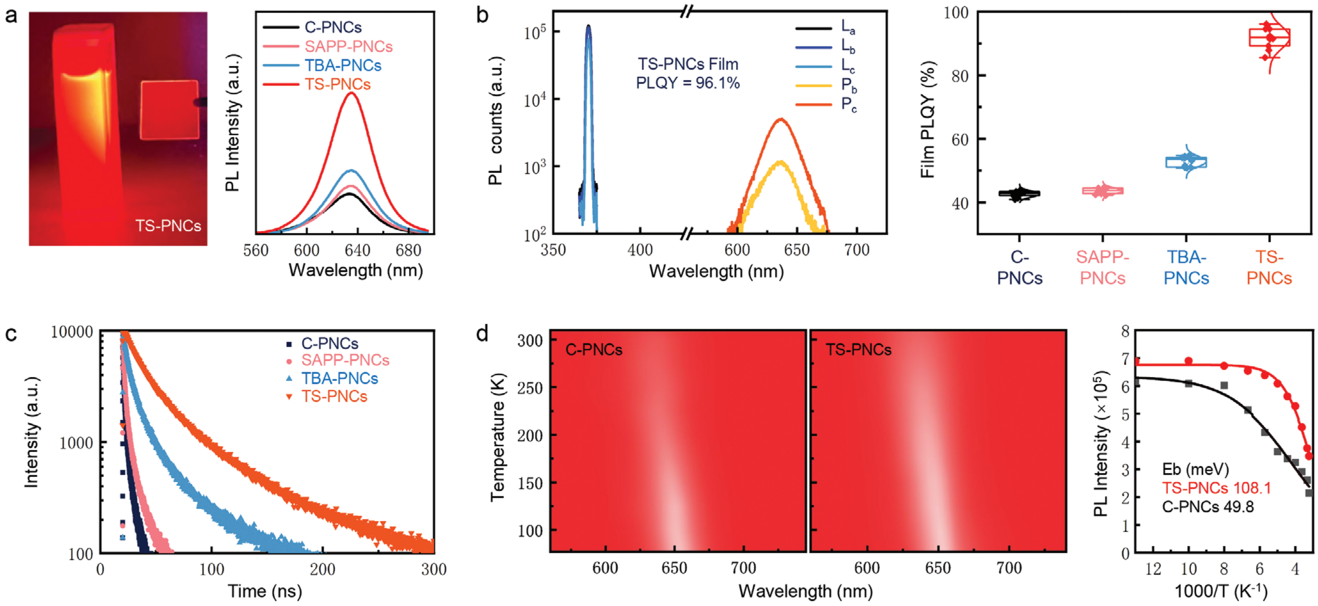

Figure 3. a) Photoluminescence of TS-PNCs dispersion and film under UV irradiation, and the PL spectra of all samples. b) PLQY of TS-PNCs films and PLQY summarization and comparisons. c) TRPL decays of C-, SAPP-, TBA-, and TS-PNCs. d) Temperature-dependent PL and fitting analysis.

photoelectron spectroscopy (UPS) analysis as depicted in Figures S21 and S22 (Supporting Information). Overall, both TBA and SAPP have successfully interacted with the surface of PNCs, effectively enhancing the adhesion of PNC films and passivating exposed Pb^{2+} defects, both of which are crucial for achieving mechanical stability and high efficiency in *F*-PLEDs.

The optical properties of the synthesized samples were systematically investigated. As shown in **Figure** 3a (left), the TS-PNCs dispersion and film exhibit a bright pure-red emission under UV irradiation, while the right delineates the PL spectra of all the samples. Compared to C-PNCs, SAPP- and TBA-PNCs demonstrate only a marginal increase in PL intensity, while TS-PNCs exhibit a markedly enhanced intensity. To quantitatively study this trend, PLQY was measured. Currently, achieving high PLQY thin films suitable for *F*-PLEDs remains a significant challenge due to the partial departure of ligands with the solvent, potentially leading to the creation of new defects. Figure 3b shows the determination of the PLQY of TS-PNCs film using an improved integrating sphere method,[42] exhibiting an impressively champion PLQY of 96.1%. The PLQY of SAPP-PNCs only increased from ≈43% to ≈45% compared to C-PNCs, due to the low solubility of SAPP. Although TBA has sufficiently high solubility, the relatively weak coordinating ability of unprotonated TBA only increases the PLQY to ≈53%. The near-unity PLQY of the TS-PNCs demonstrates the effectiveness of using three benzyl cations to carry multidentate X-type Lewis soft bases for suppressing defects. Furthermore, we explored the charge carrier dynamics through time-resolved photoluminescence (TRPL) decays, as depicted in Figure 3c, and curves were fitted with a tri-exponential function to extract parameters such as the average carrier lifetimes (τ_{avg}), as presented in Figure S23 and Table S2 (Supporting Information).[43] Remarkably, the TS ligand amplified τ_{avg} by more than tenfold and effectively mitigated the non-radiative decay rate (k_{nr}) induced by defects by about two orders of magnitude. In addition, we conducted a temperature-dependent photoluminescence analysis (Figure 3d) to investigate the impact of the TS ligand on defects and charge confinement. As the temperature increased from 77 K to 310 K, the PL spectra of PNCs gradually blue-shifted, which could be attributed to lattice thermal expansion with a positive temperature coefficient leading to bandgap widening.[44–46] Notably, as the temperature increased, exciton dissociation occurred, resulting in non-radiative trapping at defect sites, which was manifested as thermal quenching. By fitting the integrated PL intensity-dependent temperature values, the exciton binding energy (E_{eb}) values for C- and TS-PNCs were determined to be 49.8 and 108.1 meV, respectively. In summary, these results suggest that the strong coordinating effect of the TS ligand can also hinder thermal quenching, thereby enhancing the luminescent properties.

Finally, as-synthesized PNCs were incorporated into *F*-PLEDs with a device structure of AgNW/PEDOT:PSS/poly-TPD/PNCs/TPBi/LiF/Al, as depicted in Figure S24 (Supporting Information), and a comprehensive analysis of the efficiency, as well as operational and mechanical stabilities of C- and TS-*F*-PLEDs has been conducted. Figure 4a exhibits photographs of *F*-PLEDs under natural light without applied voltage and in dark with applied voltage for EL, respectively. Concurrently, Movie S1 (Supporting Information) showcases a video of the device's operation under continuous folding at various angles, demonstrating remarkable mechanical performance and operability under folding conditions. The corresponding device energy band alignment diagram is presented in the lower section of **Figure** 4a. The current density-voltage-luminescence (*J-V-L*) curves of TS-*F*-PLEDs, as shown in Figure 4b, demonstrate a reduction in the turn-on voltage from 2.5 V in C-*F*-PLEDs to 1.9 V, indicating a considerable decrease in the charge injection barrier due to the short-chain ligands structure. Furthermore, the use of TS ligands resulted in a significant enhancement in brightness, attributed to

© 2025 The Author(s). Advanced Materials published by Wiley-VCH GmbH

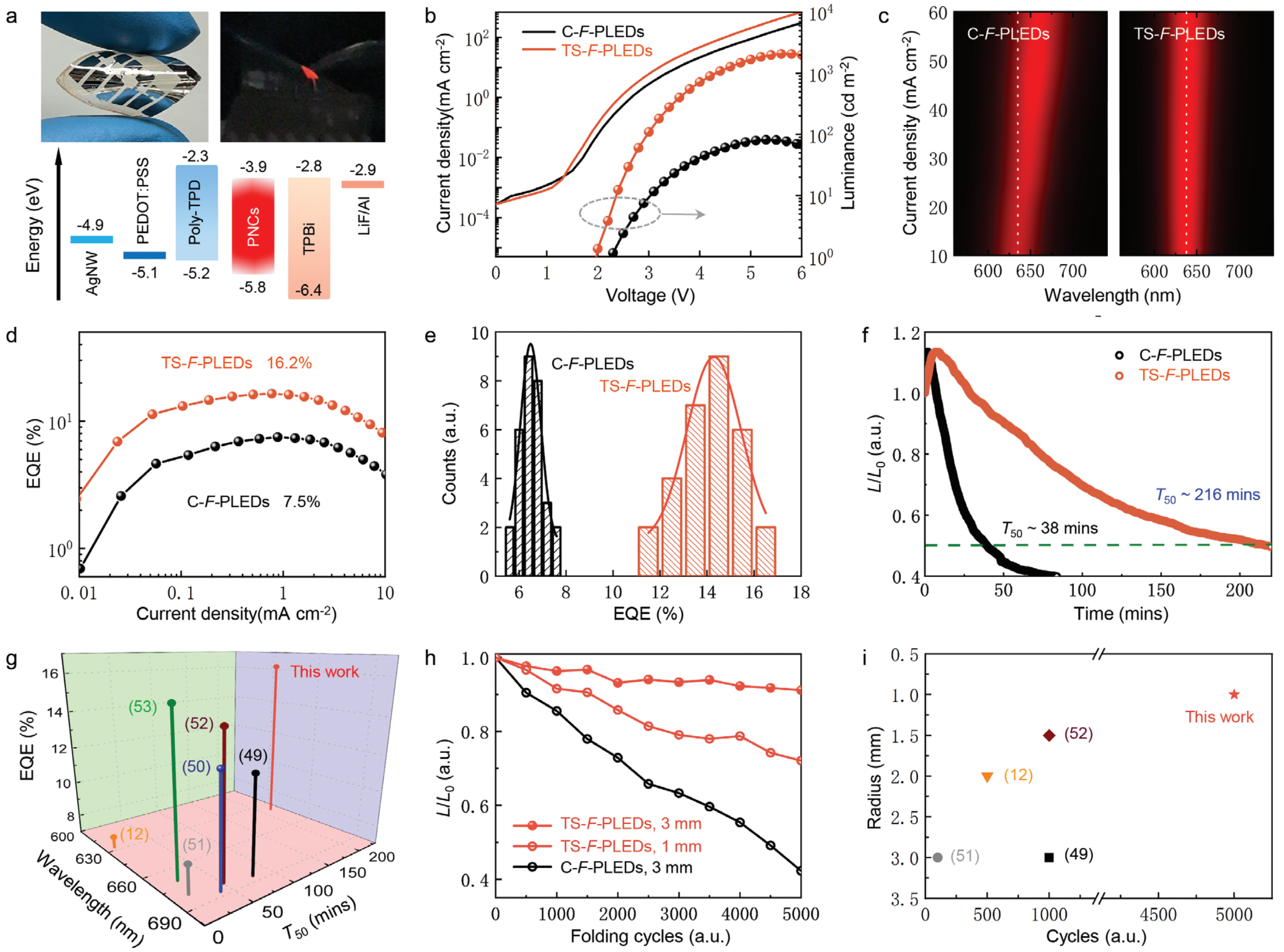

Figure 4. a) Digital photographs of *F*-PLEDs under natural light without applied voltage (left) and in dark with applied voltage (right), and the energy band alignment diagram in devices (bottom). a) *J-V-L* curves of C- and TS-*F*-PLEDs. c) EL evolution of *F*-PLEDs related to varying current densities. d) EQE of C- and TS-*F*-PLEDs. e) EQE statistics of 30 devices for both C- and TS-*F*-PLEDs. f) Operational stability comparison of C- and TS-*F*-PLEDs. g) Wavelength-EQE-T_{50} relationship for red-emitting (600–700 nm) *F*-PLEDs research in the current state-of-the-art. h) Normalized EL intensity degradation of *F*-PLEDs after folding. i) Summary of flexibility outcomes of the reported red-emitting *F*-PLEDs.

defect passivation and suppression of non-radiative recombination. These findings are further validated using the space-charge limit current method, as demonstrated in Figure S25 (Supporting Information). By fitting the *J-V* curves of double-exponential form into three regions of Ohmic (n = 1), trap-filled limited (TFL, n > 3), and Child (n = 2),[47] the trap density was extracted as 1.40 × 10^{17} and 5.39 × 10^{16}, and the electron mobility was calculated as 1.05 × 10^{-5} and 4.90 × 10^{-5} $cm^2 V^{-1} s^{-1}$ for C- and TS-PNCs based devices, respectively. At the onset of LED operation, the electroluminescence (EL) spectra peak positions for C- and TS-F-PLEDs are observed at 635 and 638 nm respectively, as depicted in Figure S26 (Supporting Information). The corresponding CIE coordinates are (0.67, 0.33) and (0.69, 0.31), respectively, as shown in Figure S27 (Supporting Information), which closely resemble the pure-red Rec. 2100 standard of (0.708, 0.292).[48] Figure 4c illustrates the EL evolution with varying current densities. Notably, TS-*F*-PLEDs maintain significantly enhanced spectral stability up to 60 mA cm^{-2}, while the emission peak of C-*F*-PLEDs exhibits a 25 nm redshift, demonstrating the greatly improved spectral stability of TS-*F*-PLEDs. Consistent with the *J-V-L* curves, the use of TS elevates the champion EQE from 7.5% to 16.2%, as illustrated in Figure 4d,e summarizes the EQE statistics of 30 devices, indicating an average EQE increase from 6.5% for C-*F*-PLEDs to 14.3% for TS-*F*-PLEDs. To the best of our knowledge, this represents the highest EQE reported for red-emitting *F*-PLEDs to date. Furthermore, the operational stability of *F*-PLEDs, a critical factor for practical applications, is substantially improved by TS with a lifetime nearly six times longer than that of C-*F*-PLEDs as depicted in Figure 4f. Thus, Figure 4g and Table S3 (Supporting Information) summarize the wavelength-EQE-T_{50} relationship for red-emitting *F*-PLEDs research in the current state-of-the-art, emphasizing the superiority of TS-*F*-PLEDs in this work.[12,49–53] It is worth mentioning that the EQE and T_{50} of *F*-PLEDs are commonly inferior to those of rigid PLEDs, underscoring the substantial scope for further research in the domain of *F*-PLEDs, including the development of high-flexibility substrates with high-temperature resistance and excellent thermal conductivity, flexible electrodes resistant to perovskite corrosion, and novel charge

© 2025 The Author(s). Advanced Materials published by Wiley-VCH GmbH

15214095, 2025, 25, Downloaded from https://advanced.onlinelibrary.wiley.com/doi/10.1002/adma.202415211, Wiley Online Library on [03/09/2025]. See the Terms and Conditions (https://onlinelibrary.wiley.com/terms-and-conditions) on Wiley Online Library for rules of use; OA articles are governed by the applicable Creative Commons License

transport layers that do not require high-temperature processing, etc.[54] The mechanical stability of *F*-PLEDs was evaluated through EL degradation after bending, as depicted in Figure 4h. The results demonstrate that TS-*F*-PLEDs exhibited exceptional mechanical resilience, retaining 93% of the initial brightness after 5000 bending cycles at a radius of 3 mm. In contrast, C-*F*-PLEDs suffered a loss of 58% of EL intensity under the same conditions, primarily due to the cracks issue observed earlier. Even at a small folding radius of 1 mm, the luminous properties of TS-*F*-PLEDs were retained at 72% after 5000 cycles, indicating their potential for future use in foldable devices. Figure 4i and Table S3 (Supporting Information) collectively summarize the flexibility outcomes of the reported red-emitting *F*-PLEDs. In conclusion, our results confirm that the TS-*F*-PLEDs not only demonstrate superior performance and operational stability but also exhibit remarkable mechanical stability.

3. Conclusion

In summary, this study has demonstrated the combination of TBA and SAPP can successfully address the challenges of mechanical instability and defect passivation in *F*-PLEDs. The ligands effectively enhanced the interlayer adhesion between PNCs and adjacent layers and also the intralayer adhesion, thereby inhibiting the formation of cracks during the folding test. Moreover, SAPP was successfully dissolved in a nonpolar solvent using TBA as a carrier, allowing for strong interaction with PNCs, as confirmed by multiple characterization approaches. The TS ligands exhibited excellent defect passivation effects, leading to a low-defect PNC thin film with excellent photoluminescence properties, including a high PLQY of up to 96.1%, a low nonradiative recombination rate, and a high exciton binding energy. Consequently, the fabricated *F*-PLEDs achieved a record-high EQE of 16.2% in the pure-red range, good spectral and operational stability, as well as robust mechanical properties capable of enduring a small folding radius of 1 mm for 5000 cycles. The strategy proposed in this study, utilizing well-designed ligand structures to enhance the mechanical stability and performance of devices, is expected to inspire further research and presents a promising pathway toward advancing the realization of high-performance and mechanically stable *F*-PLEDs.

4. Experimental Section

Synthesis of PNCs with Different Ligands: CsOA was first prepared by mixing Cs_2CO_3 (0.814 g, Solarbio, 99.90%), OA (3 ml, Aladdin, 85%), and octadecene (ODE, 30 ml, TCI, >90%) at 100 °C under vacuum for 2 h. OAmI was then synthesized by adding 0.95 ml HI solution (Acros, 57%) to a mixture of ODE (40 ml) and OAm (8 ml, Aladdin, 80–90%) under an inert atmosphere, followed by raising the temperature from room temperature to 60 °C. After 2 h, excess H_2O was removed by vacuuming. To prepare the ligands stock solution, SAPP was dried thoroughly overnight under a vacuum at 120 °C. Then, OA-OAm, SAPP, TBA, and TS were each dissolved in toluene at a concentration of 0.5 mg mL^{-1}. The mixture was refluxed at 111 °C and stirred thoroughly for 6 h, and then water was separated. In a 100 ml flask containing PbI_2 (0.09 g, Advanced Election Technology Co., ltd, >98%) and $PbBr_2$ (0.093 g, TCI, >98%), ODE (16 ml), OA (2.5 ml), and OAm (2 ml) were added, followed by 60 °C degas for 30 min, then add 4 ml of OAmI solution and degas at 100 °C for 30 min. Finally, 2 ml of CsOA was injected into the flask at 160 °C, and the PNC growth kinetics was stopped after 5 s by quenching with an ice bath. The PNCs were washed with methyl acetate (2:1 vol%) and centrifuged (6000 rpm). Then, 6 ml of toluene dissolved with various ligands was added, and the mixture was vigorously shaken on a vortex mixer for 30 min. After a further washing cycle, the purified PNCs were redispersed in 3 ml of toluene.

Fold-PLEDs Fabrication and Measurement: Ag nanowires dispersed in ethanol with a diameter of 30 nm and a length of 100–300 µm were obtained from ACS Material. Glass substrates with smooth surface roughness were cleaned using deionized water, acetone, and ethanol, and then treated with ultraviolet-ozone for 15 min. The PEDOT:PSS (Clevios PH 1000, 2% aqueous solution) and Ag nanowires were spin-coated separately onto the treated substrates.[28] The cPI (J&K) was coated onto the Ag nanowires as an ultrathin flexible substrate (<0.5 µm thickness). The samples underwent imidization processing by annealing with a gradual increase in temperature up to 200 °C. After cooling to room temperature, the glass substrate integrated PEDOT:PSS, AgNW, and cPI was submerged in deionized water and allowed to naturally delaminate to form the electrode integrated with the cPI substrate. Polydimethylsiloxane (PDMS) was used as an adhesive film to stick the peeled flexible composite electrode in the cPI flexible substrate onto the glass/PDMS as a supporting adhesive substrate. Subsequently, a hole-transporting layer of poly-TPD (4 mg mL^{-1}) was spin-coated and thermally annealed at 130 °C for 30 min. The PNCs dispersed in toluene solvent were then spin-coated onto the hole-transporting layer. Finally, TPBi, LiF, and Al were sequentially deposited by thermal evaporation under a high vacuum to complete the *F*-PLEDs. A Keithley 2635 sourcemeter and a fiber optic integration sphere (Ocean Optics FOIS-1) coupled to a spectrometer (Ocean Optics QE 65 000) were used for the LED measurements.

DFT Calculations and Finite Elemental Analysis: The adsorption configuration of SAPP- and TBA-PNCs was performed by Vienna ab initio simulation package. The DFT-D3 method was adopted to correct the van der Waals interactions. A single gamma point mesh was adopted to sample the Brillouin zone. The plane wave cutoff energy and the force convergence criterion were set to 500 eV and 0.03 eV Å^{-1}, respectively. The generalized gradient approximation of the Perdew-Burke-Ernzerhof functional was employed to describe the electron exchange-correlation interactions. More than 15 Å vacuum space was used to avoid the interaction between adjacent periodic images. The E_{ads} was estimated by the following Equation (1):

$$E_{ads} = E_{tot} - E_{sur} - E_{org} \tag{1}$$

where E_{tot} and E_{sur} represent the total energy of the PNC surface with and without organic molecule adsorption, respectively, and E_{org} is the energy of isolating organic groups, such as SAPP and TBA. The finite elemental analysis was conducted using the solid-state mechanics in COMSOL Multiphysics 5.6.

Characterization: The adhesion force and roughness of the PNC films were measured using AFM (NT-MDT NTEGRA). The bare tips were monocrystalline silicon with a curvature radius of less than 10 nm, and they were immersed in 1 mg mL^{-1} TPBi or poly-TPD solution and then thoroughly dried under a nitrogen atmosphere to get the coated tips. The SEM images were captured by Hitachi S-4800. The STEM, HRSTEM, and EDS were obtained by Thermo Scientific Talos F200X. The ATR-FTIR spectrums were recorded using JASCO FT/IR-6600 spectrometer. The XRD patterns were acquired by Bruker D8 ADVANCE Powder X-ray Diffractometer, and the X-ray source is a Siemens copper sealed tube which has a wavelength Cu Kα (λ = 1.54178 Å) with maximum Power 40 kV 40 mA while the detector is a scintillation counter. The XPS (Thermo Scientific ESCALAB 250Xi) was used for analyzing the chemical environment of elements. Steady-state PL spectra, PLQY, and TRPL were measured by PicoQuant FluoTime 300 spectrometer, and a laser diode with a peak wavelength of 375 nm was used as the excitation source. The PNC films were fabricated by spin-coating method in N_2 filled glovebox and encapsulated in two sheets of quartz sheets to avoid decomposition during PL measurement. The bending test is performed in an N2-filled glovebox with a homemade machine with linear motion guides motorized with stepper

© 2025 The Author(s). Advanced Materials published by Wiley-VCH GmbH

15214095, 2025, 25, Downloaded from https://advanced.onlinelibrary.wiley.com/doi/10.1002/adma.202415211, Wiley Online Library on [03/09/2025]. See the Terms and Conditions (https://onlinelibrary.wiley.com/terms-and-conditions) on Wiley Online Library for rules of use; OA articles are governed by the applicable Creative Commons License

15214095, 2025, 25, Downloaded from https://advanced.onlinelibrary.wiley.com/doi/10.1002/adma.202415211, Wiley Online Library on [03/09/2025]. See the Terms and Conditions (https://onlinelibrary.wiley.com/terms-and-conditions) on Wiley Online Library for rules of use; OA articles are governed by the applicable Creative Commons License

motors integrating with an Arduino home-made program to adjust the bend radius.

Calculation of PLQY The PLQY is determined using the following Equations (2) and (3):

$$PLQY = \frac{P_c - (1 - A)\,P_b}{L_a A} \tag{2}$$

$$A = 1 - \frac{L_c}{L_b} \tag{3}$$

Here, L_a represents the initial excitation, while L_b and P_b denote the excited and emitted photons from indirect illumination on the sample, respectively. L_c and P_c refer to the excited and emitted photons in the case of direct illumination.

Calculation of E_{eb} The temperature-dependent PL intensity was fitted following Arrhenius Equation (4):

$$I\ (T) = \frac{I_0}{1 + Aexp\left(-\frac{E_{eb}}{k_B T}\right)} \tag{4}$$

In the aforementioned equation, $I(T)$ and I_0 represent the PL intensity at temperature T and 0 K, respectively. A denotes the pre-exponential coefficient, and kB refers to the Boltzmann constant.

Trap density and mobility calculation

$$N_{trap} = 2\varepsilon_0 \varepsilon V_{TFL}/eL^2 \tag{5}$$

$$\mu = 8L^3 J/9\varepsilon_0 \varepsilon V^2 \tag{6}$$

In the aforementioned equations, N_{trap} represents the trap density, μ denotes the mobility, and ε_0 and ε ($\approx$4.1) represent the vacuum and relative permittivity, respectively. V_{TFL} indicates the voltage at the trap-filled limit, and e represents the elementary charge. The thickness of the PNC film is denoted by L, while J and V correspond to the current density and voltage in the Child region, respectively.[55–57]

Supporting Information

Supporting Information is available from the Wiley Online Library or from the author.

Acknowledgements

B.L. and D.L. contributed equally to this work. This work is supported by the project of the University Grant Council of the University of Hong Kong (grant No. 202111159113, and 2302101786), the General Research Fund (grant Nos. 17200021, 17200823, 17310624), Collaborative Research (grant Nos. C7035-20G) from the Research Grants Council of Hong Kong Special Administrative Region, China, and Innovation and Technology Fund (ITS/277/21FP, and GHP/245/22SZ) from Innovation and Technology Commission of Hong Kong Special Administrative Region, China.

Conflict of Interest

The authors declare no conflict of interest.

Data Availability Statement

The data that support the findings of this study are available in the supplementary material of this article.

Keywords

adhesion, foldable, ligands, light-emitting diodes, Perovskite nanocrystals

Received: October 7, 2024
Revised: January 28, 2025
Published online: March 6, 2025

[1] L. Kong, Y. Sun, B. Zhao, K. Ji, J. Feng, J. Dong, Y. Wang, Z. Liu, S. Maqbool, Y. Li, Y. Yang, L. Dai, W. Lee, C. Cho, S. D. Stranks, R. H. Friend, N. Wang, N. C. Greenham, X. Yang, *Nature* **2024**, *631*, 73.
[2] V. Morad, A. Stelmakh, M. Svyrydenko, L. G. Feld, S. C. Boehme, M. Aebli, J. Affolter, C. J. Kaul, N. J. Schrenker, S. Bals, *Nature* **2024**, *626*, 542.
[3] D. W. Kim, S. W. Kim, G. Lee, J. Yoon, S. Kim, J.-H. Hong, S.-C. Jo, U. Jeong, *Light Sci. Appl.* **2023**, *12*, 61.
[4] S. Chang, J. H. Koo, J. Yoo, M. S. Kim, M. K. Choi, D.-H. Kim, Y. M. Song, *Chem. Rev.* **2024**, *124*, 768.
[5] P. Jia, M. Lu, S. Sun, Y. Gao, R. Wang, X. Zhao, G. Sun, V. L. Colvin, W. W. Yu, *Adv. Mater. Interfaces* **2021**, *8*, 2100441.
[6] A. Liu, I. S. Mukhin, R. M. Islamova, J. Tian, *Adv. Funct. Mater.* **2024**, *34*, 2312209.
[7] J. H. Back, Y. Kwon, H. Cho, H. Lee, D. Ahn, H. J. Kim, Y. Yu, Y. Kim, W. Lee, M. S. Kwon, *Adv. Mater.* **2023**, *35*, 2204776.
[8] J. H. Jang, S. Li, D. H. Kim, J. Yang, M. K. Choi, *Adv. Electron. Mater.* **2023**, *9*, 2201271.
[9] C. Lechner, A. F. Sax, *J. Phys. Chem. C* **2014**, *118*, 20970.
[10] L. Zeng, X. Liu, X. Chen, C. Soutis, *Composites, Part B* **2021**, *220*, 108983.
[11] Y. B. Cao, D. Zhang, Q. Zhang, X. Qiu, Y. Zhou, S. Poddar, Y. Fu, Y. Zhu, J.-F. Liao, L. Shu, *Nat. Commun.* **2023**, *14*, 4611.
[12] B. Ren, D. Zhang, X. Qiu, Y. Ding, Q. Zhang, Y. Fu, J.-F. Liao, S. Poddar, C. L. J. Chan, B. Cao, C. Wang, Y. Zhou, D.-B. Kuang, H. Zeng, Z. Fan, *Sci. Adv.* **2024**, *10*, eadn1095.
[13] Y.-K. Wang, F. Jia, X. Li, S. Teale, P. Xia, Y. Liu, P. T.-s. Chan, H. Wan, Y. Hassan, M. Imran, *Sci. Adv.* **2023**, *9*, eadh2140.
[14] B. Lyu, D. Li, Q. Wang, J. Sun, Q. Xiong, D. Zhang, H. Su, W. C. Choy, *Angew. Chem., Int. Ed.* **2024**, *136*, 202408726.
[15] Y. Hassan, J. H. Park, M. L. Crawford, A. Sadhanala, J. Lee, J. C. Sadighian, E. Mosconi, R. Shivanna, E. Radicchi, M. Jeong, *Nature* **2021**, *591*, 72.
[16] D. P. Nenon, K. Pressler, J. Kang, B. A. Koscher, J. H. Olshansky, W. T. Osowiecki, M. A. Koc, L.-W. Wang, A. P. Alivisatos, *J. Am. Chem. Soc.* **2018**, *140*, 17760.
[17] D. Meggiolaro, E. Mosconi, F. De Angelis, *ACS Energy Lett.* **2019**, *4*, 779.
[18] D. Li, B. Lyu, J. Sun, Q. Xiong, H. Zhu, Z. Jiang, D. Zhang, C. Liu, W. C. Choy, *ACS Energy Lett.* **2024**, *9*, 3261.
[19] C. Li, X. Wang, E. Bi, F. Jiang, S. M. Park, Y. Li, L. Chen, Z. Wang, L. Zeng, H. Chen, *Science* **2023**, *379*, 690.
[20] B. Lyu, H. Lin, D. Li, A. Sergeev, Q. Wang, Z. Jiang, L. Huo, H. Su, K. S. Wong, Y. Wang, *ACS Energy Lett.* **2024**, *9*, 2118.
[21] L. Protesescu, S. Yakunin, M. I. Bodnarchuk, F. Krieg, R. Caputo, C. H. Hendon, R. X. Yang, A. Walsh, M. V. Kovalenko, *Nano Lett.* **2015**, *15*, 3692.
[22] Q. Zeng, X. Zhang, Q. Bing, Y. Xiong, F. Yang, H. Liu, J.-y. Liu, H. Zhang, W. Zheng, A. L. Rogach, *ACS Energy Lett.* **2022**, *7*, 1963.
[23] W. Sun, R. Yun, Y. Liu, X. Zhang, M. Yuan, L. Zhang, X. Li, *Small* **2023**, *19*, 2205950.
[24] Y. Wang, B. Li, C. Jiang, Y. Fang, P. Bai, Y. Wang, *J. Phys. Chem. C* **2021**, *125*, 16753.

© 2025 The Author(s). Advanced Materials published by Wiley-VCH GmbH

[25] H. Wang, X. Gong, D. Zhao, Y.-B. Zhao, S. Wang, J. Zhang, L. Kong, B. Wei, R. Quintero-Bermudez, O. Voznyy, *Joule* **2020**, *4*, 1977.
[26] T. Tong, B. Babatope, S. Admassie, J. Meng, O. Akwogu, W. Akande, W. Soboyejo, *J. Appl. Phys.* **2009**, *106*, 083708.
[27] J. J. Kim, K. Shuji, J. Zheng, X. He, A. Sajjad, H. Zhang, H. Su, W. C. Choy, *Nat. Commun.* **2024**, *15*, 2070.
[28] J. Kim, D. Ouyang, H. Lu, F. Ye, Y. Guo, N. Zhao, W. C. Choy, *Adv. Energy Mater.* **2020**, *10*, 1903919.
[29] Y. Wang, M. I. Dar, L. K. Ono, T. Zhang, M. Kan, Y. Li, L. Zhang, X. Wang, Y. Yang, X. Gao, *Science* **2019**, *365*, 591.
[30] H. Li, H. Lin, D. Ouyang, C. Yao, C. Li, J. Sun, Y. Song, Y. Wang, Y. Yan, Y. Wang, *Adv. Mater.* **2021**, *33*, 2008820.
[31] P. K. Jha, O. Pandey, K. Singh, *J. Mol. Struct.* **2015**, *1083*, 278.
[32] V. C. Ghantani, M. K. Dongare, S. B. Umbarkar, *RSC Adv.* **2014**, *4*, 33319.
[33] H. Li, J. Shi, J. Deng, Z. Chen, Y. Li, W. Zhao, J. Wu, H. Wu, Y. Luo, D. Li, *Adv. Mater.* **2020**, *32*, 1907396.
[34] H.-B. Yi, H. M. Lee, K. S. Kim, *J. Chem. Theory Comput.* **2009**, *5*, 1709.
[35] H. Chen, L. Fan, R. Zhang, C. Bao, H. Zhao, W. Xiang, W. Liu, G. Niu, R. Guo, L. Zhang, *Adv. Opt. Mater.* **2020**, *8*, 1901390.
[36] I. S. Zhidkov, D. W. Boukhvalov, A. F. Akbulatov, L. A. Frolova, L. D. Finkelstein, A. I. Kukharenko, S. O. Cholakh, C.-C. Chueh, P. A. Troshin, E. Z. Kurmaev, *Nano Energy* **2021**, *79*, 105421.
[37] J. K. Mishra, N. Yantara, A. Kanwat, T. Furuhashi, S. Ramesh, T. Salim, N. F. Jamaludin, B. Febriansyah, Z. E. Ooi, S. Mhaisalkar, *ACS Appl. Mater. Interfaces* **2022**, *14*, 34238.
[38] S. Gharibzadeh, B. Abdollahi Nejand, M. Jakoby, T. Abzieher, D. Hauschild, S. Moghadamzadeh, J. A. Schwenzer, P. Brenner, R. Schmager, A. A. Haghighirad, *Adv. Energy Mater.* **2019**, *9*, 1803699.
[39] S. Wang, F. Cao, Y. Wu, X. Zhang, J. Zou, Z. Lan, W. Sun, J. Wu, P. Gao, *Mater. Today Phys.* **2021**, *21*, 100543.
[40] Y. Niu, M. Xu, B. Shen, C. Dai, C. M. Li, *J. Mater. Chem. A* **2016**, *4*, 16531.
[41] Y. J. Hofstetter, I. García-Benito, F. Paulus, S. Orlandi, G. Grancini, Y. Vaynzof, *Front. Chem.* **2020**, *8*, 66.
[42] J. C. de Mello, H. F. Wittmann, R. H. Friend, *Adv. Mater.* **1997**, *9*, 230.
[43] M. Liu, Q. Wan, H. Wang, F. Carulli, X. Sun, W. Zheng, L. Kong, Q. Zhang, C. Zhang, Q. Zhang, *Nat. Photonics* **2021**, *15*, 379.
[44] H. C. Woo, J. W. Choi, J. Shin, S.-H. Chin, M. H. Ann, C.-L. Lee, *J. Phys. Chem. Lett.* **2018**, *9*, 4066.
[45] C. Yu, Z. Chen, J. J Wang, W. Pfenninger, N. Vockic, J. T. Kenney, K. Shum, *J. Appl. Phys.* **2011**, *110*, 063526.
[46] R. Saran, A. Heuer-Jungemann, A. G. Kanaras, R. J. Curry, *Adv. Opt. Mater.* **2017**, *5*, 1700231.
[47] J. S. Kim, J.-M. Heo, G.-S. Park, S.-J. Woo, C. Cho, H. J. Yun, D.-H. Kim, J. Park, S.-C. Lee, S.-H. Park, *Nature* **2022**, *611*, 688.
[48] T.-H. Han, K. Y. Jang, Y. Dong, R. H. Friend, E. H. Sargent, T.-W. Lee, *Nat. Rev. Mater.* **2022**, *7*, 757.
[49] S. Sun, P. Jia, M. Lu, P. Lu, Y. Gao, Y. Zhong, C. Tang, Y. Zhang, Z. Wu, J. Zhu, *Adv. Funct. Mater.* **2022**, *32*, 2204286.
[50] C. Chen, T. Xuan, Y. Yang, F. Huang, T. Zhou, L. Wang, R.-J. Xie, *ACS Appl. Mater. Interfaces* **2022**, *14*, 16404.
[51] F. Qin, M. Lu, S. Sun, P. Lu, N. Feng, Y. Gao, X. Bai, Z. Wu, J. Hu, Y. Zhang, *IEEE Electron Device Lett.* **2023**, *44*, 1056.
[52] F. Qin, T. Li, M. Lu, S. Sun, P. Lu, X. Li, N. Feng, Y. Zhang, Y. Gao, Z. Wu, *ACS Appl. Mater. Interfaces* **2023**, *15*, 47278.
[53] J. I. Kwon, G. Park, G. H. Lee, J. H. Jang, N. J. Sung, S. Y. Kim, J. Yoo, K. Lee, H. Ma, M. Karl, *Sci. Adv.* **2022**, *8*, eadd0697.
[54] D. Zhang, T. Huang, L. Duan, *Adv. Mater.* **2020**, *32*, 1902391.
[55] Q. Dong, Y. Fang, Y. Shao, P. Mulligan, J. Qiu, L. Cao, J. Huang, *Science* **2015**, *347*, 967.
[56] S. Sun, P. Jia, Q. Huang, M. Lu, P. Lu, F. Qin, G. Sun, Y. Gao, X. Bai, Z. Wu, *Mater. Today Phys.* **2022**, *28*, 100899.
[57] H. Shen, Q. Gao, Y. Zhang, Y. Lin, Q. Lin, Z. Li, L. Chen, Z. Zeng, X. Li, Y. Jia, *Nat. Photonics* **2019**, *13*, 192.

© 2025 The Author(s). Advanced Materials published by Wiley-VCH GmbH

15214095, 2025, 25, Downloaded from https://advanced.onlinelibrary.wiley.com/doi/10.1002/adma.202415211, Wiley Online Library on [03/09/2025]. See the Terms and Conditions (https://onlinelibrary.wiley.com/terms-and-conditions) on Wiley Online Library for rules of use; OA articles are governed by the applicable Creative Commons License